

## Mechanism study of TiO<sub>2</sub> nanowire tensile behaviors via molecular dynamics simulations

L. Dai<sup>1</sup>, V.B.C. Tan<sup>1,2</sup>, C.H. Sow<sup>1,3</sup>, C.T. Lim<sup>1,2,4</sup>, W.C.D. Cheong<sup>5</sup>

### Summary

The mechanisms governing the tensile response of TiO<sub>2</sub> nanowires were studied by molecular dynamics simulations. The free side surfaces of the nanowires were found to be undulating because atoms near the free surface were relaxed into a disordered state during thermodynamic equilibration. For wires below a threshold diameter of around 10 Å, this free surface effect extends throughout the entire wire, resulting in a complete lack of ordered structure. For thick nanowires, the core of the wire retains a crystalline structure. The thicker the wire, the larger the crystalline core and the more dominant is its effect on the tensile behavior of the wire. Under tensile loading, the initial elastic deformation is effected by the reconfiguration of surface atomic bonds. At larger extensions, the structural deformations are accomplished by continuous cycles of Ti-O bond straightening – bond breakage and inner atomic distortion – and necking until rupture. The mechanical properties of nanowires are found to be superior to those of bulk TiO<sub>2</sub>. Ultra thin nanowires, i.e., those below the threshold diameter, exhibit extraordinarily high stiffness and toughness and are more sensitive to strain rates.

Titanium dioxide (TiO<sub>2</sub>) has a wide range of applications such as in catalyst, photoelectronics, photochemistry, semiconductors and surface coatings. TiO<sub>2</sub> nanowires have been extensively studied by material researches because it is well-suited for many experimental techniques and high quality TiO<sub>2</sub> crystal materials can be directly purchased from vendors <sup>1,2</sup>. Many experimental works have been reported on the synthesis of nanowires via powder annealing <sup>3</sup>, sol-gel <sup>4,5</sup>, electrospinnning <sup>6</sup>, thermal evaporation <sup>7,8</sup> etc.. The most commonly identified crystal structure in actual TiO<sub>2</sub> nanowires are rutile <sup>3,7,8</sup> or anatase <sup>4,5,9,10</sup>.

Besides experimental works, there have also been several attempts to formulate interatomic potentials to simulate TiO<sub>2</sub> atomic interactions and nanostructures. Matsui and Akaogi <sup>11</sup> proposed a scheme with a pairwise potential plus electronic charge distribution functions to describe the atomic interactions and successfully produced the geometrical parameters of the most common crystal structures of TiO<sub>2</sub> such as rutile <sup>12</sup>, anatase <sup>13</sup>, brookite <sup>14</sup> and TiO<sub>2</sub>-II <sup>15</sup>. Swamy and Gale <sup>16</sup> introduced the quantum charge equilibration scheme <sup>17</sup> to the pairwise Morse

<sup>1</sup>NUS Nanoscience & Nanotechnology Initiative, National University of Singapore, Singapore

<sup>2</sup>Department of Mechanical Engineering, National University of Singapore, Singapore

<sup>3</sup>Department of Physics, National University of Singapore, Singapore

<sup>4</sup>Division of Bioengineering, National University of Singapore, Singapore

<sup>5</sup>Institute of materials Research and Engineering, Singapore

potential and formed an MS-Q formula. This MS-Q potential was shown to accurately describe  $\text{TiO}_2$  crystal geometries and properties<sup>18-20</sup>. However, the MS-Q potential is computationally expensive and consequently its application is limited to small scale (up to hundreds of atoms) crystalline models<sup>20</sup>. Matsui and Akaogi's scheme remains the most practical approach for comparatively large scale models and has been used to simulate  $\text{TiO}_2$  nanoparticles<sup>20</sup> and nanoclusters<sup>21,22</sup>. Here, we report on the modeling and simulation of  $\text{TiO}_2$  nanowires and elucidate the mechanisms associated with the deformation, mechanical response and ultimate rupture of  $\text{TiO}_2$  nanowires.

We use the interatomic potential of Matsui and Akaogi<sup>11</sup>, simplified as Eq-1, to describe the atomic interactions. In the equation,  $r_{ij}$  is the interatomic distance between atoms  $i$  and  $j$ ,  $q_i$ ,  $q_j$  are the electric charge of the elements, and  $A, B, C$  are fitted parameters as shown in Table-1. The Ti-O interaction is considered to predominate material structure and properties as it is much stronger than that of O-O or Ti-Ti.

$$V_{ij} = q_i q_j r_{ij}^{-1} - C r_{ij}^{-6} + A \exp\left(-\frac{r_{ij}}{B}\right) \quad (1)$$

Table 1: Parameter values for simplified Matsui and Akaogi's potential<sup>11</sup>.

$q_{Ti}$ (e)	$q_O$ (e)	$A$ (eV)	$B$ ( $\text{\AA}$ )	$C$ (eV $\text{\AA}^6$ )
2.196	-1.098	16286	0.194	1215

Molecular dynamics simulations were performed with a time step of 2 fs. The temperature was kept at 300 K throughout the simulations by scaling the atomic velocities every 500 steps. For each dynamic equilibration process, a converged system total energy and stable vibrations of atomic positions were attained to ensure the system achieved equilibrium status.

The  $\text{TiO}_2$  nanowire model was built from the most stable rutile crystalline structure with [100] aligned along the wire axis. As shown in Fig-1, the nanowire is cylindrical with a length of 59.18  $\text{\AA}$  and cross-sectional diameter of 27.6  $\text{\AA}$ , comprising a total of 3500 atoms. The atoms in the top and bottom five layers were constrained to move as two rigid blocks in a prescribed manner whereas the remaining atoms were free to displace. Firstly, the model was dynamically relaxed for 2 ns, resulting in an expansion of about 0.67% in volume as shown in Fig-2. It can be seen that the equilibration process relocated the surface atoms while the core atomic arrangement remained unchanged.

With the equilibrated structure, the tensile process was simulated in a quasi-static manner: The top and bottom five layers of atoms were prescribed to displace 0.5  $\text{\AA}$  upwards and downwards individually, i.e. a 1  $\text{\AA}$  longitudinal stretch, within each time step. The free atoms were then dynamically equilibrated for 500 ps before the next stretch. These stretching-equilibration iterations gave an equivalent

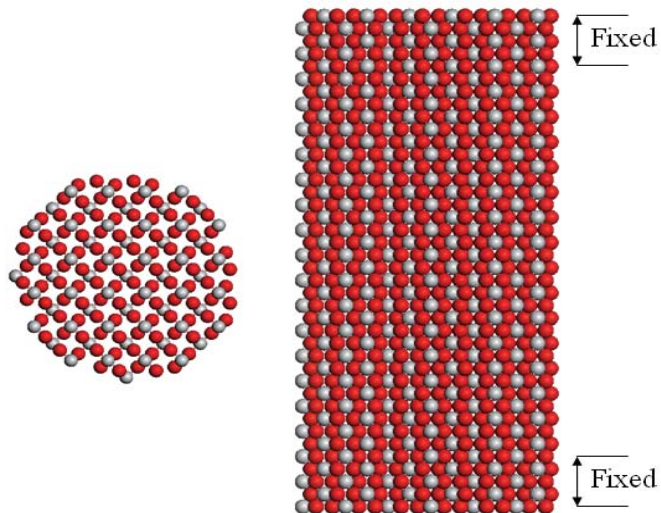


Figure 1: Cross sectional (left) and longitudinal (right) views of cylindrical TiO<sub>2</sub> nanowire model containing 3500 atoms before equilibration.

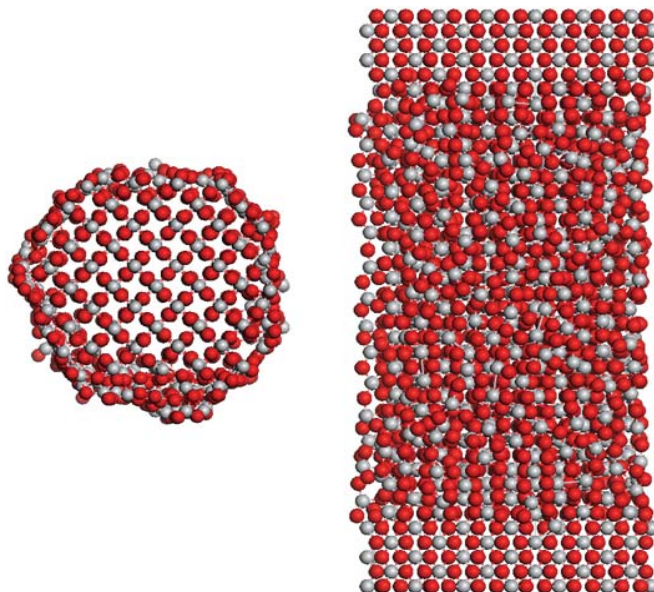


Figure 2: Cross sectional (left) and longitudinal (right) views of equilibrated cylindrical TiO<sub>2</sub> nanowire model. The relaxed surface atoms comprises about 39.4% of the total free atoms.

0.2 m/s stretch rate and were repeated for 33 times until the rupture of the nanowire.

The snapshots of tensile process are presented in Fig-3. At the initial stage

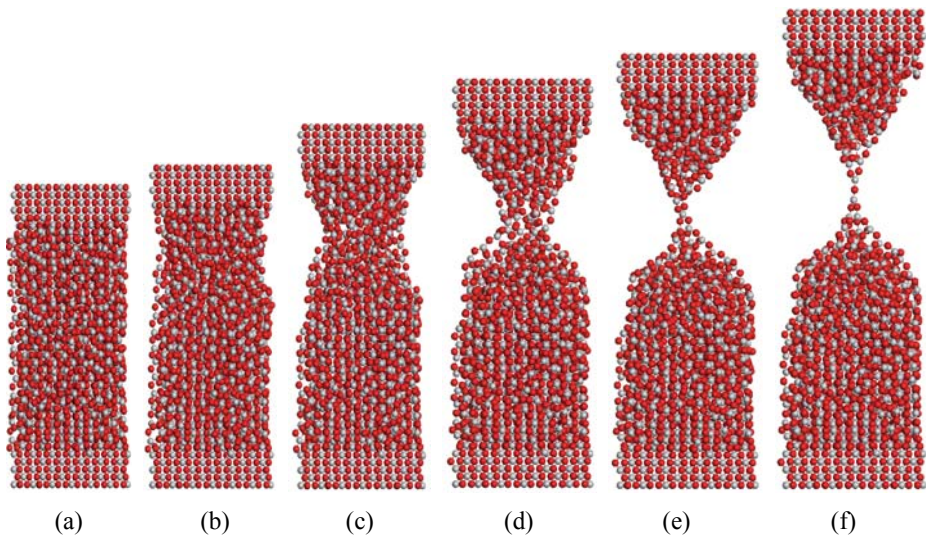


Figure 3: Tensile loading of  $\text{TiO}_2$  nanowire at strain levels of (a) 1.6%, (b) 8.4%, (c) 20%, (d) 35.2%, (e) 43.6% and (f) 53.7%.

of the simulations, the nanowire stretched elastically. At a strain of 8.4%, atomic rearrangement was observed and necking became apparent. With further stretching, the neck became thinner and thinner until a single-atom-neck (Fig-3f) is observed prior to rupture.

In order identify the mechanisms behind the observations, the tensile behavior was analyzed by examining the atomic re-arrangement together with the calculated tensile stress and statistics of Ti-O bonds.

Fig-4 shows a section of the [110] crystalline surface that comprises the nanowire axis. Based on the rutile crystal structure, each Ti atom is bonded to six O atoms in either the [110] or [-110] surface to form a  $\text{Ti}_3\text{O}_6$  unit, i.e. two horizontally adjacent units are presented in Fig-4. The left of the figure is the free surface of the cylindrical nanowire and the right is towards the centerline of the wire. The atoms within the dashed box, not including the two O atoms bonded to Ti-3 (Ti atoms are numbered as 1-5) in [-110] surface, were chosen for presenting the atomic rearrangements under tensile loading.

The continuous tensile-induced atomic re-arrangement occurred in five stages as presented in Fig-5 - initial equilibration (chart a), yielding (chart b), ultimate tensile stress (UTS) (chart c) and two plastic necking deformations (charts d and e).

Fig-5a shows the initial equilibrated wire prior to stretching. The configuration of the surface atoms (Ti-1 and Ti-2 group) were relaxed due to the free surface

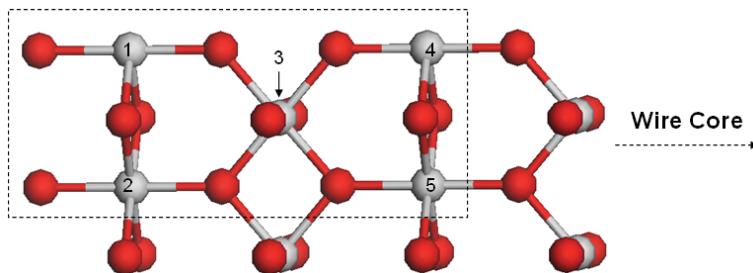


Figure 4: Two units of  $Ti_3O_6$  of the [110] rutile crystalline structure. The view is rotated slightly to show the  $O$  atoms on the [-110] surface. Red denotes  $O$  atoms and grey denotes  $Ti$  atoms.

conditions while the inner atomic arrangement (Ti-3 and Ti-4 group) retained the crystalline structure.

At the start of the tensile loading, stretching at the wire surface atoms caused the Ti-1 and Ti-2 groups to move apart, while the inner atomic bonds only experienced small uniform elastic strain (Fig-5b). The breaking of the  $O$  bond with Ti-2 marked the beginning of irreversible strain and was considered as the onset of yielding.

As the Ti-1 and Ti-2 groups were further pulled apart accompanied by the straightening of the  $Ti$ - $O$  bonds (Fig-5c), the initiation of necking was observed (Fig-3b). This also initiated the deformation of inner atoms in the form of bond rotations between the Ti-4 and Ti-5 atoms (Fig-5d).

When the load exceeded the bond strength between the  $O$  atoms and the Ti-3 and Ti-5 atoms, more  $Ti$ - $O$  bonds broke and a new surface was created (Fig-5e). This was observed as a shrinking of the necked region (Fig-3c). The Ti-2 group then separated from the Ti-3 group (Fig-5e) but both groups remained tied to other neighboring atoms. It was noted that as free surface area increased together with more dangling bonds, some new bonds were formed arbitrarily. The bonds at the new surface were subsequently straightened under further stretching resulting in a stage similar to that shown in Fig-5b. Thus, the stretching of the wire occurs through continuous cycles of bond straightening – bond breakage and inner atomic distortion – neck shrinking until the formation of a single-atom-neck prior to eventual rupture.

The tensile stress of the nanowire was calculated as the virial stress and the stress-strain curve is plotted in Fig-6a together with three snapshots (I to III) of representative atomic arrangements. Snapshots I and II are top views taken at the yielding and UTS stages whereas snapshot III is the longitudinal view of the final single-atom-neck phenomenon. Fig-6b shows how the number of  $Ti$ - $O$  bonds

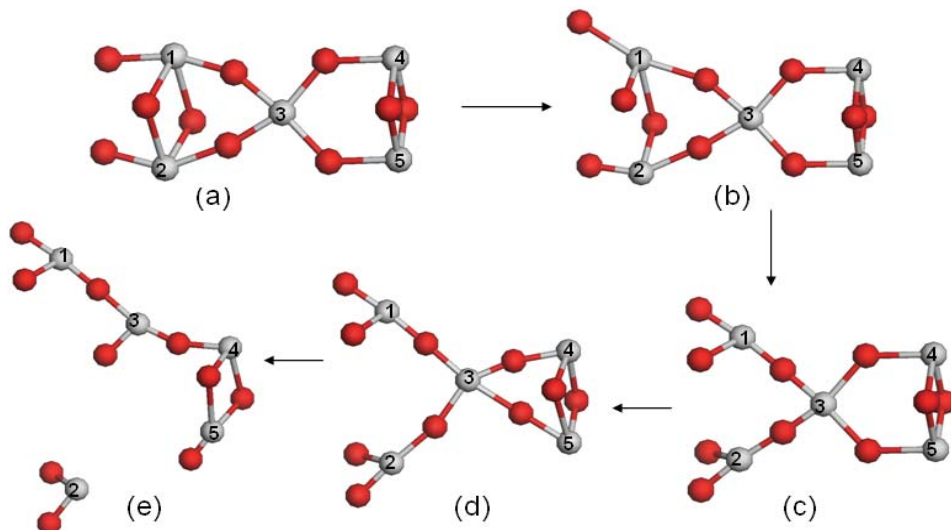


Figure 5: Atomic re-arrangement of atoms within the dashed box of Fig-4 under tensile loading, (a) initial equilibration, (b) yielding, (c) ultimate tensile stress, (d) and (e) necking.

decreased as the wire is stretched. Fig-6c is the plot of the Ti-O bond lengths to give an indication of the bond strength at different stages. Fig-6d is the plot of the projection of bond lengths onto the longitudinal direction of the wire because the longitudinal component contributes to the stiffness and toughness of the nanowire. Since the mechanical properties of the wire are determined by the localized necking region after yielding, only the atoms within upper section of the nanowire where necking occurred (1312 atoms) were accounted for in Figs. 6b, 6c and 6d.

At the initial stage of the tensile loading, the number of Ti-O bonds (Fig-6b) remained unchanged, showing that the deformation at this stage was purely due to bond stretching and rotation. Fig-6c and Fig-6d present a trend of Ti-O bond straightening in the longitude direction, indicating an increasing tensile stress. From the stress-strain curve (Fig-6a), we can see an initial linear stage, where the slope gives a Young's modulus of 304 GPa. This is higher than that of experimental measurement (287.9 GPa<sup>23</sup>) and the calculated value for polycrystalline bulk using the approach described by Hashin-Shtrikman<sup>24</sup> (277 GPa).

The yield point occurred at around 1.7% strain and a tensile stress of 5.1 GPa (Fig-6a). Irreversible bond breakage was confined to the surface Ti-O bonds while the inner core maintained the rutile crystalline arrangement (snapshot-I in Fig-6a).

Beyond the yielding stage, the upward trend of both the total (Fig-6c) and longitudinal component (Fig-6d) of the Ti-O bond length corresponded with the increase in tensile stress until the UTS. The UTS was calculated to be 8.15 GPa,

a value much higher than experimental measurements<sup>25</sup> of between 54.88 MPa (3-7% porosity) and 58.8 MPa (density 4100 kg/m<sup>3</sup>). As the surface bonds were straightened upon reaching UTS, continued loading started to influence the inner atoms and gave rise to the distortion of inner crystals (snapshot-II, Fig-6a).

With further stretching, the Ti-O bonds at the interface of the surface atoms and inner crystalline core (Ti-3 group in Fig-5d) could no longer sustain the tensile load. Thus, more Ti-O bonds were broken and a new surface was created. The structure momentarily relaxed to a new state of atomic re-arrangement. Accordingly, the number of Ti-O bonds dropped (Fig-6b) and the bond stiffness decreased (Fig-6c and d). Together with the structural relaxation, the tensile stress dropped significantly (Fig-6a).

Afterwards, the tensile loading resulted in continuous cycles of bond straightening – bond breakage and inner atomic distortion – neck shrinkage. Accordingly, the curves in Fig-6a-d showed oscillations before the final rupture. The oscillations occurred together with a general downward trend in tensile stress as shown in Figs-6a and 6d. Finally, a single-atom-neck was formed at 48.7% strain and rupture occurred at 55.4% strain. The evolution of the necking region to a single-atom-neck configuration suggests that the nanowire is very ductile and presents the possibility of producing very thin wires.

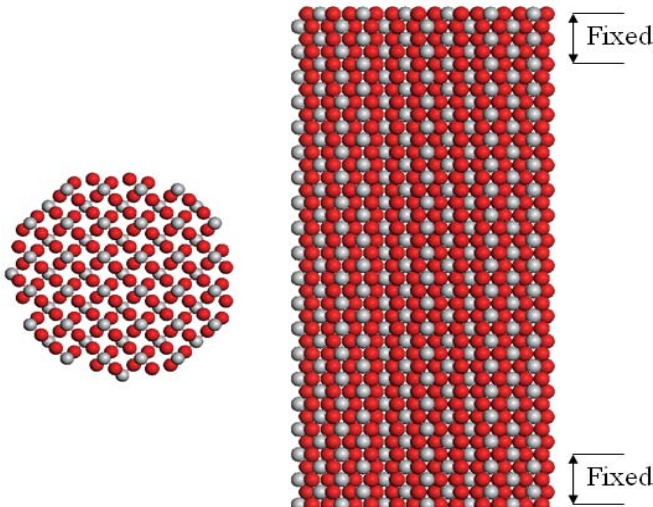
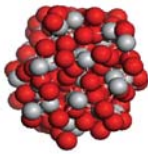
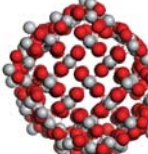
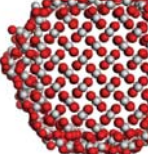
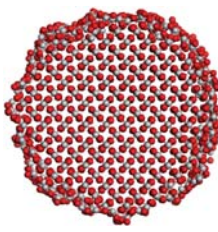


Figure 6: Plots of (a) Stress-strain curve (b) number of Ti-O bonds (c) average length of Ti-O bonds (d) average length of Ti-O bonds projected onto the longitudinal direction. In chart (a), the three insets from left to right show the atomic arrangements at yielding, just beyond UTS and the single-atom-neck. In charts (b), (c) and (d) only atoms within the necking region (1312 atoms) are considered.

In order to obtain a better understanding of the free surface effects on the tensile behavior of the TiO<sub>2</sub> nanowires, three more nanowires with different diameters were simulated. Table-2 shows the cross-sectional diameter, concentration of free side surface atoms and top view of total all four nanowires. The results presented thus far are for model III. When the diameter was below 10 Å, as for nanowire I, all the free atoms were relaxed into a disordered state after thermal equilibration at 300 K. This phenomenon was also reported as non-linear effects<sup>26,27</sup> and has also been found for nanowires of other materials, like metals<sup>28,29</sup>, silicon<sup>30</sup> and other metal oxides<sup>31,32</sup>. In all cases, a similar threshold of around 10 Å for the diameter was notified. This strongly suggests that the phenomenon is common to all inorganic nanowires because the lattice constant of most crystals are of several angstroms, and the free surface conditions were observed to affect a size of a few crystal lattices. For thicker nanowires, the free side surface effect is limited to the outer skin while the inner core maintained their crystalline configuration.

Table 2: Concentrations of free side surface effect on TiO<sub>2</sub> nanowire models of different cross-sectional diameters.

Number	I	II	III	IV
Diameter (Å)	9.2	18.4	27.6	46.0
Percentage of atoms affected by free surface	100%	61.2%	39.4%	21.6%
Top view at equilibration				

The same stepwise tensile loading was simulated for the three additional nanowires I, II and IV, and their stress-strain curves are presented in Fig-7. It can be seen that thinner nanowire is stiffer and stronger. In nanowire I, some relaxed Ti-O bonds were rotated and straightened longitudinally during the initial elastic stage, and the UTS of 23.06 GPa was attained at a strain of 3.3%. This gives an extraordinarily high value of Young's modulus of 688.3 GPa. Thereafter, tensile deformation was mainly accomplished via the straightening of the nanowire and extensive vibrating plastic stresses were observed. Nanowires III and IV exhibited similar mechanical responses, both elastically and plastically, despite their size difference, indicating a

converged size effect.

Therefore, the size effect for ultra thin  $TiO_2$  nanowires is due to the large percentage of relaxed free surface atoms, which significantly transforms the structure and enhances the stiffness and toughness of the nanowire. When the nanowire thickness is larger than the threshold value of around 10 Å, a crystalline structure appears at the core of the wire. With increasing wire thickness, the crystalline structure becomes dominant and the mechanical properties of the wire approach those of the bulk  $TiO_2$ . Fig-8 plots Young's modulus and UTS versus nanowire thickness based on our available data. It is seen that the Young's modulus converges to a value equal to that calculated for bulk  $TiO_2$ . The UTS of defect free  $TiO_2$  nanowire with a rutile crystalline structure can thus be expected to be 6.8 GPa from the same figure.

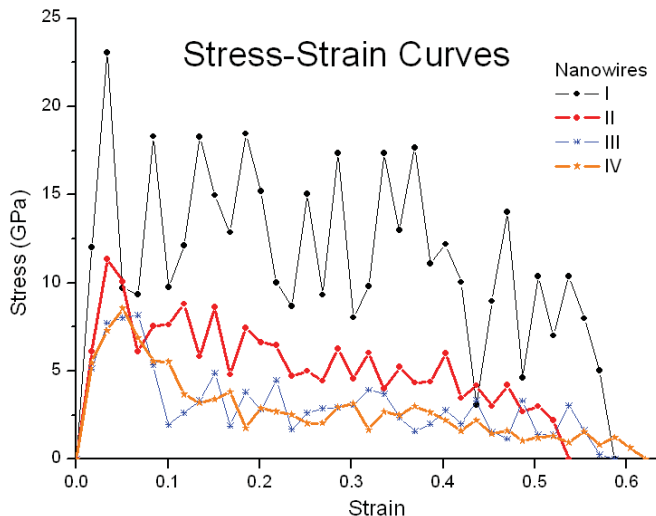


Figure 7: Tensile stress-strain curves for the four nanowires with different thickness.

We also found that the thinner a nanowire is, the longer is the time required for equilibration per stepwise stretch. In models III and IV of the nanowires, 200 ps of relaxation for every stepwise stretch of 1 Å was sufficient for equilibration, giving an equivalent stretch rate of 0.5 m/s. For the thinner nanowires, models I and II, longer time intervals were required for equilibration. The equivalent rates of stretching for model II and the even thinner model I were 0.4 m/s and 0.2 m/s respectively. These minimum stretch rates for stable simulations suggest that thin nanowires are more strain rate sensitive than thicker ones.

In conclusion our simulation results revealed that:

1. The free surface effects dictate the structure and property of ultra thin  $TiO_2$

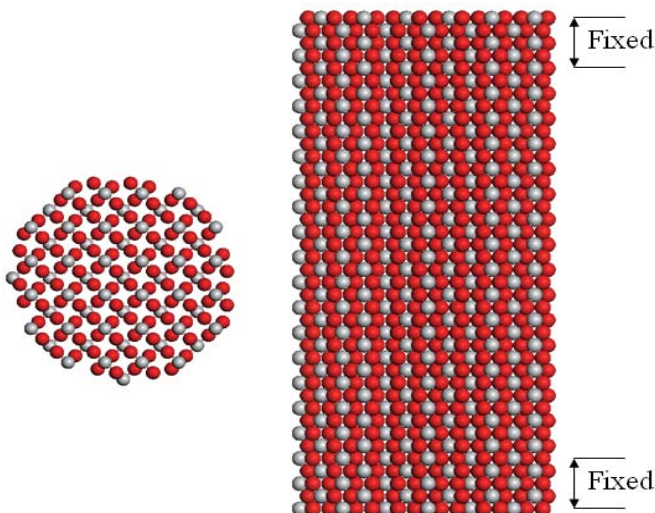


Figure 8: Plots Young's modulus and UTS as functions of nanowire thickness.

nanowires. The atoms at the surface of a nanowire equilibrate into a relaxed, disordered state and causes the reconfiguration of the entire nanowire structure when the cross-sectional diameter is below the threshold of around 10 Å. For thicker nanowires, a crystalline structure is conserved within the wire core after thermal dynamic equilibration.

2. Under stepwise tensile loading, the surface atoms are displaced by bond rotation and straightening prior to the breaking of Ti-O bonds. For nanowires with equilibrated crystalline cores, the plastic tensile deformation occurs as continuous cycles of Ti-O bond straightening – bond breakage and inner atomic distortion – neck shrinkage until rupture.
3. Compared to the bulk materials,  $\text{TiO}_2$  nanowires are found to be stiffer and superior in terms of toughness and ductility. Ultrathin nanowires, in particular, with their high concentration of free surface atoms, are extremely stiff and strong. They also require lower strain rates in order to attain equilibration after each step of stretching.

## References

1. Diebold, U. *Surf. Sci. Reports* **2003**, 48, 53.
2. Lu, J. G.; Chang, P. C.; Fan, Z. Y. *Mater. Sci. Eng. R* **2006**, 52, 49.
3. Li, G. L.; Wang, G. H. *J. Mater. Res.* **1999**, 14, 3346.
4. Miao, Z.; Xu, D. S.; Ouyang, J. H.; Guo, G. L.; Zhao, X. S.; Tang, Y. Q. *Nano Lett.* **2002**, 2, 717.

5. Miao, L.; Tanemura, S.; Toh, S.; kaneko, K.; Tanemura, M. *J. Cryst. Grow.* **2004**, 264, 246.
6. Li, D.; Xia, Y. N. *Nano Lett.* **2003**, 3, 555.
7. Wu, J. M.; Shih, H. C.; Wu, W. T.; Tseng, Y. K.; Chen, I. C. *J. Cryst. Grow.* **2005**, 281, 384.
8. Wu, J. M.; Shih, H. C.; Wu, W. T. *Nanotechnology* **2006**, 17, 105.
9. Arlt, T.; Bermejo, M.; Blanco, M. A.; Gerward, L.; Jiang, J. Z. *Phys. Rev. B* **2000**, 61, 14414.
10. Wen, B. M.; Liu, C. Y.; Liu, Y. *Inorg. Chem.* **2005**, 44, 6503.
11. Matsui, M.; Akaogi, M. *Mol. Sim.* **1991**, 6, (4), 239.
12. Abrahams, S. C.; Bernstein, J. L. *J. Chem. Phys.* **1971**, 55, 3206.
13. Burdett, J. K.; T.Hughbanks; Miller, G. J.; Richardson, J. W.; Smith, J. V. *J. Am. Chem. Soc.* **1987**, 109, 3639.
14. Meagher, E. P.; Lager, G. A. *Canad. Mineral.* **1979**, 17, 77.
15. Simons, P. Y.; Dachille, F. *Acta Cryst.* **1967**, 23, 334.
16. Swamy, V.; Gale, J. D. *Phys. Rev. B* **2000**, 62, (9).
17. Rappe, A. K.; III, W. A. G. *J. Phys. Chem.* **1991**, 95, 3358-3363.
18. Swamy, V.; Gale, J. D.; Dubrovinsky, L. S. *J. Phys. Chem. Solids* **2001**, 62,
19. Thomas, B. S.; Marks, N. A.; Begg, B. D. *Phys. Rev. B* **2004**, 69.
20. Hallil, A.; Tetot, R.; Berthier, F.; Braems, I.; Creuze, J. *Phys. Rev. B* **2006**, 73.
21. Collins, D. R.; Smith, W.; Harrison, N. M.; Forester, T. R. *J. Mater. Chem.* **1996**, 6, 1385.
22. Filyukov, D. V.; Brodskaya, E. N.; Piotrovskaya, E. M.; Leeuw, S. W. d. *Russ. J. Gen. Chem.* **2007**, 77, 10.
23. Isaak, D. G.; Garnes, J. D.; Anderson, O. L.; Cynn, H.; Hake, E. *Phys. Chem. Minerals* **1998**, 26, 31.
24. Cheong, F. C.; Varghese, B.; Zhu, Y. W.; Tan, E. P. S.; Dai, L.; Tan, V. B. C.; Lim, C. T.; Sow, C. H. *J. Phys. Chem. C* **2007**, 111, 17193.
25. Samsony, G. V., *The Oxide Handbook*. second ed.; New York - Washington - London, 1982.
26. Burki, J.; Stafford, C. A. *Appl. Phys. A* **2005**, 81, 1519.
27. Liang, H. Y.; Upmanyu, M. *Phys. Rev. B* **2005**, 71, 241403.

28. Diao, J. K.; Gall, K.; Dunn, M. L. *J. Mech. Phys. Solids* **2004**, 52, 1935.
29. HafTEL, M. I.; Gall, K. *Phys. Rev. B* **2006**, 74, 035420.
30. Zhao, Y. F.; Yakobson, B. I. *Phys. Rev. Lett.* **2003**, 91, 035501.
31. Zhang, L. X.; Huang, H. C. *Appl. Phys. Lett.* **2007**, 90, 023115.
32. Kulkarni, A. J.; Zhou, M. *Appl. Phys. Lett.* **2006**, 88,